

Observations of a magnetic dip in a quiescent prominence foot

Huadong Chen (✉ hdchen@nao.cas.cn)

National Astronomical Observatories, Chinese Academy of Sciences <https://orcid.org/0000-0001-6076-9370>

Suli Ma

National Space Science Center, Chinese Academy of Sciences

Yingna Su

Key Laboratory of DMSA, Purple Mountain Observatory, Chinese Academy of Sciences

Guiping Zhou

Eric Priest

University of St Andrews <https://orcid.org/0000-0003-3621-6690>

Yuandeng Shen

Yunnan Observatories <https://orcid.org/0000-0001-9493-4418>

Chun Xia

Yunnan University

Weining Tu

Astronomy Department, Beijing Normal University

Lyndsay Fletcher

University of Glasgow <https://orcid.org/0000-0001-9315-7899>

Jun Zhang

School of Physics and Materials Science, Anhui University

Article

Keywords:

Posted Date: February 22nd, 2022

DOI: <https://doi.org/10.21203/rs.3.rs-1305619/v1>

License:   This work is licensed under a Creative Commons Attribution 4.0 International License.

[Read Full License](#)

Observations of a magnetic dip in a quiescent prominence foot

HUADONG CHEN ^{1,2} SULI MA ^{3,1} YINGNA SU ⁴ GUIPING ZHOU ^{1,2} ERIC PRIEST ⁵ YUANDENG SHEN ⁶
CHUN XIA ⁷ WEINING TU,⁸ LYNDISAY FLETCHER ^{9,10} AND JUN ZHANG^{11,1}

¹*National Astronomical Observatories, Chinese Academy of Sciences, Beijing 100101, People's Republic of China*

²*School of Astronomy and Space Science, University of Chinese Academy of Sciences, Beijing 100049, People's Republic of China*

³*National Space Science Center, Chinese Academy of Sciences, Beijing 100190, People's Republic of China*

⁴*Key Laboratory of DMSA, Purple Mountain Observatory, Chinese Academy of Sciences, Nanjing 210008, People's Republic of China*

⁵*School of Mathematics and Statistics, University of St Andrews, St Andrews, Fife KY16 9SS, UK*

⁶*Yunnan Observatories, Chinese Academy of Sciences, Kunming 650216, People's Republic of China*

⁷*School of Physics and Astronomy, Yunnan University, Kunming 650500, People's Republic of China*

⁸*Astronomy Department, Beijing Normal University, Beijing 100875, People's Republic of China*

⁹*SUPA School of Physics and Astronomy, University of Glasgow, Glasgow, G12 8QQ, UK*

¹⁰*Oslo Rosseland Centre for Solar Physics University of Oslo, P.O.Box 1029 Blindern, NO-0315 Oslo, Norway*

¹¹*School of Physics and Materials Science, Anhui University, Hefei 230601, People's Republic of China*

ABSTRACT

Solar prominences (or filaments) are cooler and denser plasma suspended in the much hotter and rarefied solar corona. When viewed on the solar disc filament barbs or feet protrude laterally from filament spine. When viewed at solar limb, they extend down to the chromosphere. For a long time, the magnetic field orientation of barbs has remained a mystery due to the paradox that the barbs possess vertical fine structures and flows but are likely to be supported in a horizontal magnetic field. Here we present highly suggestive observations of a magnetic dip in a quiescent prominence foot with an upward-curved field. That is indicated by the horizontal bidirectional outflows probably produced by magnetic reconnection between the fields of a tiny erupting filament and those in a prominence foot. The observations shed light on the field structure of prominences which is crucial for the instability that accounts for the eruption of prominences and coronal mass ejections.

1. INTRODUCTION

The magnetic structure of solar prominences or filaments is a key issue in solar physics. It is important not only for understanding how the prominence mass is supported in the corona, but also for clarifying the instability mechanisms of filament eruptions and the effects of eruptive filaments on space weather. Direct field measurements of prominences are rare and arduous to make and interpret¹. They have shown that quiescent prominences mostly possess horizontal magnetic fields with a field strength of 10–20 G on average¹ and an inclination angle of $\sim 40^\circ$ to the long axis of the prominence^{2–4}.

Regarding the magnetic nature of filaments, the magnetic structure of filament barbs protruding laterally from the spine is most controversial^{5,6}. It has been demonstrated that the end points of filament barbs are close to small parasitic magnetic fields on each side of filaments⁷, but their detailed association is not yet fully clear. Vertical fine structure and vertical flows are often observed in prominence feet at the limb. Assuming that the flows of filament plasma are guided by magnetic field, some studies suggest that the field lines in barbs are predominantly vertical and directly connect filament spines to the photosphere⁸, while other observations indicate that prominence feet may harbor helical magnetic fields connecting the prominence to the solar surface^{9,10}.

However, the observed velocities of the up- or down-flows in filament barbs are about 10 km s^{-1} , much less than the free-fall speeds corresponding to the filament heights^{8,11} which would be expected for vertical flows along magnetic

field lines. H_α Doppler shift observations from Meudon observatory indicate that the velocity vectors of the apparent vertical flows in a quiescent prominence have substantial horizontal components¹². On the other hand, the vertical extent of a barb is much larger than the gravitational scale height of prominence plasma (~ 200 km), also implying that the prominence plasma must somehow be supported against gravity. Using the idea of magnetic dips, some linear or nonlinear force-free flux rope models^{13–16} have successfully produced three-dimensional configurations of filaments that can naturally explain the morphology of both filament spines and barbs. According to the models, barbs represent cool matter residing in small dips, which are caused by the local distortion of a large-scale flux rope due to the introduction of parasitic polarities onto a large-scale bipolar photospheric flux distribution. This produces secondary photospheric inversion lines around the parasitic magnetic elements, and is supported by results from the comparison of Big Bear Solar Observatory (BBSO) H_α images with magnetograms taken by SOHO MDI¹⁷.

Many results from theoretical models and observations tend to support the idea that the vertical structure of prominence feet or filament barbs may represent a pile up of dips in more or less horizontal magnetic field lines^{18–23}. However, to date, clear observations of magnetic dip structures in prominence feet have not been presented^{24–28}. Here, we remedy this by analyzing a filament eruption event on 2014 April 8, during which a small erupting filament first interacted with a magnetic arcade under a large-scale prominence foot and then appeared to reconnect with the overlying fields of the prominence foot. A second reconnection produced bright bidirectional outflows moving along upwardly curving paths with respect to the local horizontal line in UV and EUV intensity images, which strongly suggest a magnetic dip structure across the prominence foot.

2. OBSERVATIONS

The minor eruption event occurred at the southeast limb of the Sun, and was well observed by the Atmospheric Imaging Assembly (AIA)²⁹ of the Solar Dynamics Observatory (SDO) and the Interface Region Imaging Spectrograph (IRIS)³⁰ (see Fig. 2 and Fig. 3). In this event, a small erupting filament “EF” collided and interacted with a nearby quiescent prominence’s foot. By checking the successive AIA EUV and Kanzelhöhe Solar Observatory (KSO) H_α observations from April 8 to April 13, we found that the prominence foot corresponds to a barb structure. Figure 1 shows the filament barbs (“Barb1” and “Barb2”) on the disk on April 13 and the corresponding prominence feet at the limb on April 8. EF in the event was close to Barb1 (Fig. 1e). In the AIA EUV hot lines, the large-scale filament structure is not clear, but the dark filament channel is visible. A line-of-sight magnetogram from the Helioseismic and Magnetic Imager (HMI)³¹ on board SDO shows the weak quiescent photospheric magnetic fields on both sides of the filament channel. The AIA 171 Å intensity image enhanced by the Multiscale Gaussian Normalization (MGN) method³² in Fig. 1f shows that there is a multitude of dip structures across the barbs’ tops and in the vertical threads of Barb1, similar to previous observations³³.

Figures 2 and 3 show the details of the small filament eruption in the AIA EUV and IRIS UV lines, respectively. Prior to the eruption, we can see an arcade structure (“Ar”) and a small cavity below Barb1, which is reminiscent of the prominence bubbles that are often observed under prominences³⁴ and filament barbs^{22,35}. The eruptive filament EF is very small and is hardly visible before it erupted. The eruption started at about 07:30 UT on April 8. As the EF expanded outwards, it first encountered the Ar and interacted with it. Two obvious brightenings (“Brs”) appeared almost simultaneously at the intersection of EF and Ar and at one end of Ar (marked by the two circles in Fig. 2c), suggesting a magnetic reconnection between the fields of the EF and Ar. The brightening at the Ar’s end was likely caused either by thermal conduction or by energy released, e.g. fast electrons, in the reconnection region.

As the Br at the reconnection region was pushed aside, EF continued to erupt upwards and then collided with the overlying prominence material and magnetic fields in Barb1, during which reconnection probably occurred again. In the AIA 304 Å and 171 Å lines, we have detected simultaneous bidirectional outflows from the second reconnection region, which are called two-sided-loop jets in some studies^{36,37}. Some absorption features (indicated by the black arrow in Fig. 2h) in the vertical threads of Barb1 are observed to be disturbed and to move behind the bright outflows in the 171 Å intensity images. The outflows are invisible in the hotter AIA channels, such as the 193 Å, 211 Å and 335 Å, implying that the highest temperature of the plasma in the outflows may be about 0.6 MK, which is the temperature response peak of the 171 Å channel. The IRIS slit-jaw imager (SJI) 1400 Å data with higher spatial resolution ($\sim 0''.33$) shows the bidirectional outflows from the second reconnection region more clearly (Fig. 3). It can be seen that several groups of bidirectional outflows successively took place due to reconnection between the fields of EF and Barb1. Figure 3d–i show three examples of outflows. Most importantly, we found that the outflows gradually curved upwards relative to the local horizontal orientations. Assuming the magnetic field is frozen in to the plasma,

the upward-curved trajectories of the outflows strongly suggest that some magnetic dip fields existed and crossed the vertical structures in Barb1. Besides the vertical dark threads of Barb1 in AIA 171 Å, some horizontal structures in front of the foot in AIA 304 Å or IRIS 2796 Å are observed to be disturbed by the filament eruption, suggesting that some fields close to Barb1 may also participate in the reconnection with the EF.

Along the slit A–B (see Fig. 2e) and a curved slit C–D (see Fig. 3g), we produced AIA 304 Å and IRIS 1400 Å time-distance diagrams in Fig. 4a and Fig. 4d, respectively. They separately show the dynamics of the small erupting filament EF, its overlying prominence material in Barb1 and the bidirectional outflows. It can be seen that as EF erupted upwards, its overlying prominence material was compressed and forced to rise by about 10 Mm and then stopped. The temporal profiles of the projected velocity and acceleration of EF (red) and the overlying prominence material (blue) are presented in Fig. 4b and 4c, respectively. EF underwent a rapid-acceleration phase with a maximum acceleration of $0.27 \pm 0.07 \text{ km s}^{-2}$ after the eruption onset. At about 07:36 UT, EF reached a maximum speed of $56 \pm 3 \text{ km s}^{-1}$ and then was decelerated probably due to confinement by the overlying magnetic structures and prominence material. After 07:48 UT, EF gradually faded out of the AIA 304 Å images. Six pairs of outflows (“o1”–“o6” in Fig. 4d) are identified in the IRIS 1400 Å time-slit map, which has been enhanced by the MGN method. Applying linear fits to the outflow trajectories in the time-distance map, we found that the projected velocities of the outflows moving towards C are on average larger than those of the outflows towards D. Their average values are $85 \pm 2 \text{ km s}^{-1}$ and $62 \pm 2 \text{ km s}^{-1}$, respectively. The difference in outflow velocity along the two directions is probably due to the asymmetry in ambient outflow conditions, with that in the downflow region being denser.

Some outflows towards C were captured by the IRIS spectrometer slit, which is marked by the vertical black lines in the IRIS UV intensity images (Fig. 3). We mainly analyzed the spectra of the Si IV 1394 Å line to deduce the spectral characteristics of the outflows. The 1394 Å spectral line is formed at a temperature of $\sim 0.08 \text{ MK}$. After doing absolute wavelength calibration, we applied a single-Gaussian fit to the spectral data and obtained the temporal evolutions of the peak intensity, Doppler shift, and line width from 07:43 to 08:10 UT, which are separately displayed in the top three panels of Fig. 5. It can be seen that the first outflow crossed the IRIS slit at about 07:45 UT. Subsequently, multiple outflows followed the first one and passed through the approximately same position of the spectrometer slit. The Doppler speeds of the outflows had significant blueshift signatures ($[-5, -18] \text{ km s}^{-1}$) before 07:55 UT and then exhibited redshifts ($[7, 20] \text{ km s}^{-1}$), suggesting that different dipped field lines participated in the reconnection with the EF. The average Doppler speed is $\sim 11 \text{ km s}^{-1}$, much less than the projected velocities ($\sim 85 \text{ km s}^{-1}$) of the outflows, suggesting that the outflows are located close to the plane of the sky. The Doppler line widths vary in the range $[5, 16] \text{ km s}^{-1}$ with a mean value of $\sim 10 \text{ km s}^{-1}$, and a mean nonthermal velocity of $\sim 6 \text{ km s}^{-1}$ probably due to turbulence or unresolved Alfvén waves in the outflows³⁸. The IRIS SJI 1400 Å intensity images of the two outflows at 07:51 and 08:08 UT and the corresponding Si IV 1394 Å line spectra and line profiles are plotted in the bottom panels of Fig. 5. It can be seen that the 1394 Å spectral line is separately blueshifted by $\sim 13 \text{ km s}^{-1}$ and redshifted by $\sim 20 \text{ km s}^{-1}$ for the two outflows.

Figuring out the magnetic characteristics of the dip fields in the lateral feet is helpful and important for understanding the magnetic structure and equilibrium of the prominences. Generally, the prominence material is heated by magnetic reconnection to tens of thousands or millions of degrees and so would become fully ionized, which leads to a high electrical conductivity of the heated plasma. It is likely that the outflows under investigation were ejected from the reconnection region and moved along the magnetic fields because of the frozen-in condition. Since the Doppler speeds of the outflows are much smaller than the projected speeds, the motion trajectories of the outflows approximately reflect the real configuration of the magnetic dip fields. In Fig. 6a, we draw the trajectory of the outflow observed by IRIS at 07:56:17 UT (see Fig. 3g) on the background of a simultaneous KSO H_α intensity image. Here, we established a cartesian system of coordinates, where the z -axis refers to the vertical axis of Barb1, the y -axis points to us, and the x -axis represents the horizontal direction perpendicular to Barb1. The altitude (height) of the bottom of the dip is estimated to be $\sim 30 \text{ Mm}$. The angles φ between the dip field and the x -axis were calculated and plotted in Fig. 6b. The mean value of φ at the edge of Barb1 is $3.9^\circ \pm 0.4^\circ$, which are denoted by the plus signs and vertical dashed lines in Fig. 6. We also calculated the curvature radii projected in the plane of the sky of the dip bottom, with a mean value of $73 \pm 9 \text{ Mm}$.

Before reconnection, the equilibrium of the prominence material in Barb1 is approximately governed by the magnetohydrostatic force balance equation³⁹

$$0 = -\nabla p - \rho g \hat{z} - \nabla \left(\frac{B^2}{2\mu} \right) + (\mathbf{B} \cdot \nabla) \left(\frac{\mathbf{B}}{\mu} \right). \quad (1)$$

Here, p , ρ , g , μ and B are the gas pressure, mass density, solar gravitational acceleration, magnetic permeability and magnetic field strength, respectively. At the edges of Barb1, the z -component of Eq. (1) implies in order of magnitude that

$$\rho g \approx \frac{2B_x B_z}{\mu w}, \quad (2)$$

where w is the width of Barb1 and B_x is assumed uniform. Replacing B_z with $B_x \tan \varphi$, evaluated at the edge of the barb, this implies that

$$\rho g \mu w \approx 2B_x^2 \tan \varphi. \quad (3)$$

Given that the electron density⁴⁰ and ionization degree⁴¹ of the prominence is $2.4 \times 10^{10} \text{ cm}^{-3}$ and ~ 0.3 , respectively, then $\rho \approx 1.3 \times 10^{-10} \text{ kg m}^{-3}$. Coupled with $w \approx 9700 \text{ km}$ and $\varphi \approx 4^\circ$, this implies that $B_z \approx 1 \text{ G}$, and $B_x \approx 18 \text{ G}$, which is a typical field strength for quiescent prominences^{4,42}.

3. DISCUSSION

Whether a magnetic dip exists in filament barbs or prominence lateral feet has been a matter of debate for many years. Some direct magnetic or velocity vector field measurements^{4,43,44} of prominences suggest that horizontal magnetic components may indeed exist in prominence feet. The vertical fine structure of prominence feet may then be an accumulation of magnetic dipoles, which are well reproduced in some theoretical models^{13,15,45}. Observationally, however, up to now, any conspicuous dip configurations across prominence feet have not yet been detected and presented. In this study, using high-resolution imaging and spectroscopy data from IRIS and SDO, we clearly demonstrate a magnetic dip structure in or near a quiescent prominence foot, which shows up as upwardly-curved trajectories of simultaneous bidirectional outflows (or jets) driven by the reconnection between the fields of a small erupting filament and those of or close to a prominence foot. The results provide highly suggestive observational evidence for dip fields in prominence feet or filament barbs. On the other hand, there may also be vertical fields extending down to the photosphere in prominence foot. In the AIA 304 Å and IRIS UV imaging data, a small arcade Ar appeared at the bottom of Barb1, implying that some fields may come out from the ends of Ar and pass upwards through Barb1.

As for the dip fields in the foot, when and how they formed and what their relationship is to the prominence fields, are still not clear. Some theoretical studies have modeled filament barbs forming from parasitic polarities interacting with the filament spine^{14,15}. Moreover, the reconnection between the approaching opposite polarity legs of different sheared magnetic arcades along a filament channel may also produce such dipped fields^{46–50}. When cool and dense plasma accumulates in such dipped fields by injection or condensation, a filament barb or prominence foot may be created. In this scenario, a magnetic arcade naturally appears below the dip after the reconnection, consistent with the observations presented here. In Fig. 7a and b, we have plotted the possible magnetic field structure on the lower part of a large-scale filament. The flux rope has two groups of dipped fields, which correspond to the two barbs Barb1 and Barb2, respectively. Some fields (dashed lines in the diagram) may be anchored in the photosphere around the barbs. Fig. 7c–e show the eruption of the small filament EF and its two reconnections separately with Ar and the overlying dip fields in Barb1. The heated plasma was rapidly expelled from the second reconnection region and flowed along the dip fields in Barb1 to form the bright outflows, as observed by IRIS and SDO/AIA.

4. METHODS

Dynamics of the erupting filament EF and the bidirectional outflows. Using the AIA 304 Å data, we first find the source region center (indicated by the plus signs in Fig. 2) of the erupting filament. Then, we connect the center and the top edge of EF to give the filament eruption direction. Slit A–B goes through the source region center and along the eruption direction. The evolution of the top edge of the EF and the overlying prominence material compressed by the EF are shown in the AIA 304 Å time-distance diagram made along the slit A–B (see Fig. 4a). According to the moving features of the EF and the overlying material in the time-height map, we separately choose 12 and 9 data points and calculate their first and second derivatives. The corresponding velocities and accelerations of EF and the overlying material are plotted in Fig. 4b and c. Along the motion trajectory of the outflow observed by IRIS at 07:56:17 UT, we use a relatively wide ($\sim 3.7 \text{ Mm}$) curved slit CD (see Fig. 3g) to make the 1400 Å time-slit map (Fig. 4d). Six pairs of bidirectional outflow features are selected from the 1400 Å time-slit image and linear fittings are applied to them to obtain the outflow velocities, which are shown in Fig. 4e.

Analysis of the IRIS spectra of the outflows. For this event, the IRIS spectral data are taken in a sit-and-stare raster mode with 9 second cadence and a spectral resolution of $\sim 0.025 \text{ Å}$. Because the event occurred at the solar limb,

the usual method⁵¹ using the neutral lines such as O I 1355.5977 Å and Fe II 1392.817 Å, is not applicable for absolute wavelength calibration. As shown in Fig. 3, the spectrometer slit mainly covered the prominence foot which stayed relatively stable during the observation. The difference between the centroid of the total 1394 Å line profile averaged over the whole slit and 1393.78 Å is utilized for the absolute wavelength calibration of the Si IV 1394 Å line spectra. A slight blueshift of ~ 2 km s⁻¹ is found from this wavelength calibration method. After the absolute wavelength calibration, we applied a single-Gaussian fit to the spectral data and obtained the temporal evolutions of the peak intensity, Doppler shift, and line width of the Si IV 1394 Å spectral line (see Fig. 5a–c). The Si IV 1394 Å line spectra and profiles of the outflows at 07:51:29 and 08:08:34 UT are plotted in Fig. 5d–f and Fig. 5g–i, respectively.

5. DATA AVAILABILITY

The observational data from IRIS, SDO and KSO used for the figures are available at <https://iris.lmsal.com/search/>, <http://jsoc.stanford.edu/ajax/lookdata.html>, and <http://cesar.kso.ac.at/halpha3a/2014/>, respectively.

6. REFERENCES

1. Vial, J.-C. & Engvold, O. *Solar Prominences* Vol. 415 (Springer, 2015).
2. Bommier, V. & Leroy, J. L. Global pattern of the magnetic field vector above neutral lines from 1974 to 1982: Pic-du-Midi observations of prominences. In *IAU Colloquium 167: New Perspectives on Solar Prominences*, *Astronomical Society of the Pacific Conference Series* Vol. 150 (eds Webb, D. F. et al.) 434–438 (Astronomical Society of the Pacific, 1998).
3. Schmieder, B., López Ariste, A., Levens, P., Labrosse, N. & Dalmasse, K. Polarimetric measurements in prominences and “tornadoes” observed by THEMIS. In *IAU Symposium: Polarimetry: From the Sun to Stars and Stellar Environments*, *Proceedings IAU Symposium No. 305* (eds Nagendra, K. N. et al.) 275–281 (International Astronomical Union, 2015).
4. Mackay, D. H., Schmieder, B., López Ariste, A. & Su, Y. Modelling and observations: Comparison of the magnetic field properties in a prominence. *Astron. Astrophys.* 637, A3 (2020).
5. Xia, C., Keppens, R., Antolin, P. & Porth, O. Simulating the in situ condensation process of solar prominences. *Astrophys. J. Lett.* 792, L38 (2014).
6. Ouyang, Y., Chen, P. F., Fan, S. Q., Li, B. & Xu, A. A. Does a solar filament barb always correspond to a prominence foot? *Astrophys. J.* 894, 64 (2020).
7. Martin, S. F. Conditions for the formation and maintenance of filaments (invited review). *Sol. Phys.* 182, 107–137 (1998).
8. Zirker, J. B., Engvold, O. & Martin, S. F. Counter-streaming gas flows in solar prominences as evidence for vertical magnetic fields. *Nature* 396, 440–441 (1998).
9. Su, Y., Wang, T. J., Veronig, A., Temmer, M. & Gan, W. Q. Solar magnetized “tornadoes:” relation to filaments. *Astrophys. J. Lett.* 756, L41 (2012).
10. Martínez González, M. J., Manso Sainz, R., Asensio Ramos, A., Beck, C., de la Cruz Rodríguez, J. & Díaz, A. J. Spectro-polarimetric imaging reveals helical magnetic fields in solar prominence feet. *Astrophys. J.* 802, 3 (2015).
11. Shen, Y. D., Liu, Y., Liu, Y. D., Chen, P. F., Su, J. T., Xu, Z. & Liu, Z. Fine magnetic structure and origin of counter-streaming mass flows in a quiescent solar prominence. *Astrophys. J. Lett.* 814, L17 (2015).
12. Schmieder, B., Chandra, R., Berlicki, A. & Mein, P. Velocity vectors of a quiescent prominence observed by Hinode/SOT and the MSDP (Meudon). *Astron. Astrophys.* 514, A68 (2010).
13. Aulanier, G. & Démoulin, P. 3-D magnetic configurations supporting prominences (I. The natural presence of lateral feet). *Astron. Astrophys.* 329, 1125–1137 (1998).
14. Aulanier, G., Démoulin, P., van Driel-Gesztelyi, L., Mein, P. & DeForest, C. 3-D magnetic configurations supporting prominences (II. The lateral feet as a perturbation of a twisted flux-tube). *Astron. Astrophys.* 335, 309–322 (1998).
15. van Ballegooijen, A. A. Observations and modeling of a filament on the sun. *Astrophys. J.* 612, 519–529 (2004).
16. Su, Y. N. & van Ballegooijen, A. A. Observations and magnetic field modeling of a solar polar crown prominence. *Astrophys. J.* 757, 168 (2012).
17. Chae, J., Moon, Y.-J. & Park, Y.-D. The magnetic structure of filament barbs. *Astrophys. J.* 626, 574–578 (2005).
18. López Ariste, A., Aulanier, G., Schmieder, B. & Sainz Dalda, A. First observation of bald patches in a filament channel and at a barb endpoint. *Astron. Astrophys.* 456, 725–735 (2006).

19. Dudík, J., Aulanier, G., Schmieder, B., Zapiór, M. & Heinzel, P. Magnetic topology of bubbles in quiescent prominences, *Astrophys. J.* 761, 9 (2012).
20. Li, L. P. & Zhang, J. The evolution of barbs of a polar crown filament observed by SDO. *Sol. Phys.* 282, 147–174 (2013).
21. Gunár, S., Dudík, J., Aulanier, G., Schmieder, B. & Heinzel, P. Importance of the H_{α} visibility and projection effects for the interpretation of prominence fine-structure observations. *Astrophys. J.* 867, 115 (2018).
22. Guo, Y. L., Hou, Y. J., Li, T. & Zhang, J. Reconstructing 3D magnetic topology of on-disk prominence bubbles from stereoscopic observations. *Astrophys. J. Lett.* 911, L9 (2021).
23. Barczynski, K., Schmieder, B., Peat, A. W., Labrosse, N., Mein, P. & Mein, N. Spectro-imagery of an active tornado-like prominence: Formation and evolution. *Astron. Astrophys.* 653, A94 (2021).
24. Labrosse, N., Heinzel, P., Vial J.-C., Kucera, T., Parenti, S., Gunár, S., Schmieder, B. & Kilper, G. Physics of solar prominences: I—spectral diagnostics and non-LTE modelling. *Space Sci. Rev.* 151, 243–332 (2010).
25. Mackay, D. H., Karpen, J. T., Ballester, J. L., Schmieder, B. & Aulanier, G. Physics of solar prominences: II—magnetic structure and dynamics. *Space Sci. Rev.* 151, 333–399 (2010).
26. Parenti, S. Solar prominences: Observations. *Living Rev. Sol. Phys.* 11, 1 (2014).
27. Gibson, S. E. Solar prominences: theory and models fleshing out the magnetic skeleton. *Living Rev. Sol. Phys.* 15, 7 (2018).
28. Chen, P. F., Xu, A.-A. & Ding, M. D. Some interesting topics provoked by the solar filament research in the past decade. *Research in Astron. Astrophys.* Vol. 20 No. 10, 166 (2020).
29. Lemen, J. R. et al. The Atmospheric Imaging Assembly (AIA) on the Solar Dynamics Observatory (SDO). *Sol. Phys.* 275, 17–40 (2012).
30. De Pontieu, B. et al. The Interface Region Imaging Spectrograph (IRIS). *Sol. Phys.* 289, 27332779 (2014).
31. Schou, J. et al. Design and ground calibration of the Helioseismic and Magnetic Imager (HMI) instrument on the Solar Dynamics Observatory (SDO). *Sol. Phys.* 275, 229–259 (2012).
32. Morgan, H. & Druckmüller, M. Multi-scale gaussian normalization for solar image processing. *Sol. Phys.* 289, 2945–2955 (2014).
33. Su, Y. N., van Ballegooijen, A. A., McCauley, P., Ji, H. S., Reeves, K. K. & DeLuca, E. E. Magnetic structure and dynamics of the erupting solar polar crown prominence on 2021 March 12. *Astrophys. J.* 807, 144 (2015).
34. Berger, T., Testa, P., Hillier, A., Boerner, P., Low, B. C., Shibata, K., Schrijver, C., Tarbell, T. & Title, A. Magneto-thermal convection in solar prominences. *Nature* 472, 197–200 (2011).
35. Martin, S. F., Panasenco, O., Agah, Y., Engvold, O. & Lin, Y. Relating a prominence observed from the Solar Optical Telescope on the Hinode satellite to known 3-D structures of filaments. *The Second Hinode Science Meeting, Astronomical Society of the Pacific Conference Series* Vol. 415 (eds Lites, B. et al.) 183–187 (Astronomical Society of the Pacific, 2009).
36. Yokoyama, T. & Shibata, K. Magnetic reconnection as the origin of X-ray jets and H_{α} surges on the Sun. *Nature* 375, 42–44 (1995).
37. Shen, Y. D., Qu, Z. N., Yuan, D., Chen, H. D., Duan, Y. D., Zhou, C. R., Tang, Z. H., Huang, J. & Liu, Y. Stereoscopic observations of an erupting mini-filament-driven two-sided-loop jet and the applications for diagnosing a filament magnetic field. *Astrophys. J.* 883, 104 (2019).
38. Tian, H. et al. Prevalence of small-scale jets from the networks of the solar transition region and chromosphere. *Science* 346, 1255711 (2014).
39. Priest, E. *Magnetohydrodynamics of the Sun* (Cambridge Univ. Press, 2014).
40. Chen, H. D., Zhang, J., De Pontieu, B., Ma, S. L., Kliem, B. & Priest, E. Coronal mini-jets in an activated solar tornado-like prominence. *Astrophys. J.* 899, 19 (2020).
41. Anzer, U. & Heinzel, P. Is the magnetic field in quiescent prominences force-free? *Astron. Astrophys.* 467, 1285–1288 (2007).
42. Bommier, V., Leroy, J. L. & Sahal-Bréchet, S. The linear polarization of hydrogen H_{β} radiation and the joint diagnostic of magnetic field vector and electron density in quiescent prominences. *Astron. Astrophys.* 156, 79–89 (1986).
43. Levens, P. J., Schmieder, B., López Ariste, A., Labrosse, N., Dalmasse, K. & Gelly, B. Magnetic field in atypical prominences structures: bubble, tornado, and eruption. *Astrophys. J.* 826, 164 (2016).

- 294 44. Schmieder, B., Zapiór, M., López Ariste, A., Levens, P., Labrosse, N. & Gravet, R. Reconstruction of a helical
 295 prominence in 3D from IRIS spectra and images. *Astron. Astrophys.* 606, A30 (2017).
- 296 45. Luna, M., Su, Y., Schmieder, B., Chandra, R. & Kucera, T. A. Large-amplitude longitudinal oscillations triggered
 297 by the merging of two solar filaments: observations and magnetic field analysis. *Astrophys. J.* 850, 143 (2017).
- 298 46. van Ballegoijen, A. A. & Martens, P. C. H. Formation and eruption of solar prominences. *Astrophys. J.* 343,
 299 971–984 (1989).
- 300 47. Martens, P. C. & Zwaan, C. Origin and evolution of filament-prominence systems. *Astrophys. J.* 558, 872–887
 301 (2001).
- 302 48. Xia, C., Keppens, R. & Guo, Y. Three-dimensional prominence-hosting magnetic configurations: creating a
 303 helical magnetic flux rope. *Astrophys. J.* 780, 130 (2014).
- 304 49. Chen, H. D., Zhang, J. Cheng, X., Ma, S. L., Yang, S. H. & Li, T. Direct observations of tether-cutting
 305 reconnection during a major solar event from 2014 February 24 to 25. *Astrophys. J. Lett.* 797, L15 (2014).
- 306 50. Yan, X. L., Xue, Z. K., Pan, G. M., Wang, J. C., Xiang, Y. Y., Kong, D. F. & Yang, L. H. The formation and
 307 magnetic structures of active-region filaments observed by NVST, SDO, and Hinode. *Astrophys. J. Suppl. Ser.* 219,
 308 17 (2015).
- 309 51. Tian, H., Young, P. R., Reeves, K. K., Chen, B., Liu, W. & McKillop, S. Temporal evolution of chromospheric
 310 evaporation: case studies of the M1.1 flare on 2014 September 6 and X1.6 flare on 2014 September 10. *Astrophys. J.*
 311 811, 139 (2015).

312 7. ACKNOWLEDGEMENTS

313 H.D.C., Y.N.S. and S.L.M. were supported by the National Key R&D Program of China 2021YFA1600502 and
 314 2021YFA1600503 (2021YFA1600500). H.D.C. and G.P.Z. were supported by the Strategic Priority Research Program
 315 of Chinese Academy of Sciences, Grant No. XDB 41000000. H.D.C. and J.Z. acknowledge the NSFC support from grant
 316 numbers 11790304, 11790300 and 12073001 and the Key Programs of the Chinese Academy of Sciences (QYZDJ-SSW-
 317 SLH050). S.L.M. was also supported by the NSFC (11790301 and 11941003). Y.N.S. also acknowledges the support of
 318 NSFC (11790302, 11790300 and 41761134088). G.P.Z. was also supported by the NSFC (11873059), the Key Research
 319 Program of Frontier Sciences, CAS (grant No. ZDBS-LY-SLH013), and Beijing Natural Science Foundation 1202022,
 320 and Yunnan Academician Workstation of Wang Jingxiu (No. 202005AF150025). Y.D.S acknowledges the NSFC
 321 support (12173083, 11922307 and 11773068) and the Yunnan Science Foundation for Distinguished Young Scholars
 322 (202101AV070004). C.X. acknowledges the NSFC support (11803031, 12073022) and the Basic Research Program of
 323 Yunnan Province (2019FB140, 202001AW070011). L.F. acknowledges support from the UK Research and Innovation's
 324 Science and Technology Facilities Council under grant award number ST/T000422/1. IRIS is a NASA small explorer
 325 mission developed and operated by LMSAL with mission operations executed at NASA Ames Research center and
 326 major contributions to downlink communications funded by ESA and the Norwegian Space Centre. The SDO data are
 327 courtesy of NASA, the SDO/AIA, and SDO/HMI science teams. The H-alpha data were provided by the Kanzelhöhe
 328 Observatory, University of Graz, Austria.

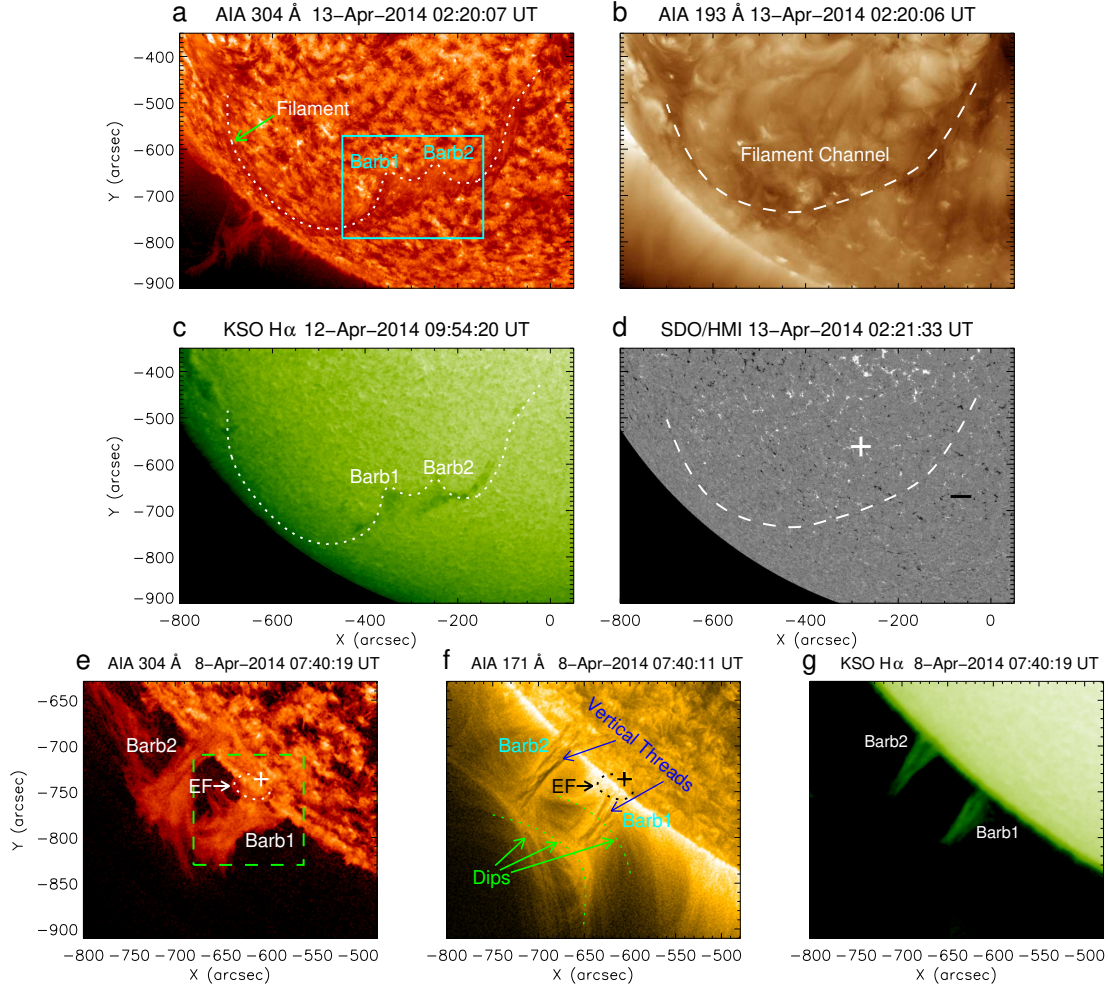


Figure 1. SDO and KSO observation of the large-scale filament and associated line-of-sight photospheric magnetic fields. **a**, SDO AIA 304 Å intensity data at $T = 0.05$ MK on April 13 show that the filament had a spine structure with two apparent barbs (Barb1 and Barb2). The box in **a** approximately indicates the field of view (FOV) of panels **e**, **f** and **g**. **b**, The dark filament channel is displayed in the AIA 193 Å intensity image at $T = 1.5$ MK (also 20 MK). **c**, Similar to **a**, but for KSO $H\alpha$ intensity data at $T < 0.01$ MK, which has been de-rotated to the time April 13 02:20 UT. **d**, Line-of-sight photospheric magnetogram observed by SDO HMI. The plus and minus sign in **d** represent the major positive and negative magnetic fields on the two sides of the filament, respectively. **e**, The two barbs in the AIA 304 Å line appeared as two vertical feet of a prominence at the solar limb on April 8. The dashed rectangle in **e** corresponds to the FOV of Fig. 2. **f** and **g**, Similar to **e**, but in the AIA 171 Å (at $T = 0.6$ MK) and KSO $H\alpha$ waveband, respectively. “EF” in **e** and **f** refer to a small-scale erupting filament. The location of EF eruption source is denoted by the plus signs in **e** and **f**. See Supplementary Video 1.

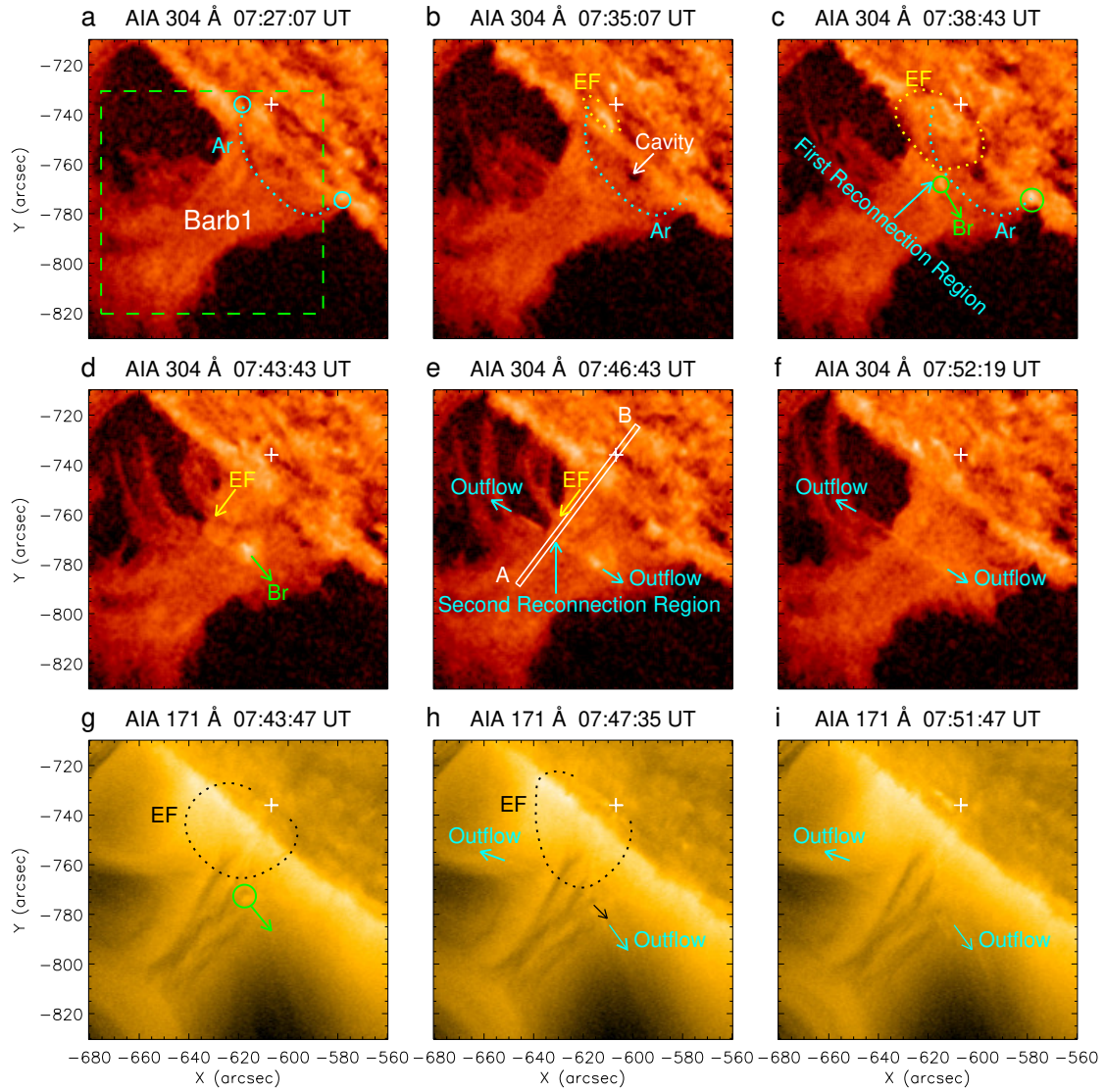


Figure 2. SDO AIA observation of the EF eruption event on 2014 April 8. **a–f**, EF interacting with arcade Ar and Barb1 in the AIA 304 Å channel at $T = 0.05$ MK. The square in **a** shows the FOV of panels **a–c** of Fig.3. The circles in **a** indicate the two footpoints of Ar. The circles in **c** denote the brightenings (Brs) due to the interaction between EF and Ar. The narrow box in **e** is the slit “A–B” along which the AIA 304 Å time-distance diagram was plotted in panel **a** of Fig. 4. **g–i**, The interaction of EF and Barb1 in the AIA 171 Å line at $T = 0.6$ MK. The plus signs in the diagram indicate the source region of the eruption. See Supplementary Video 2.

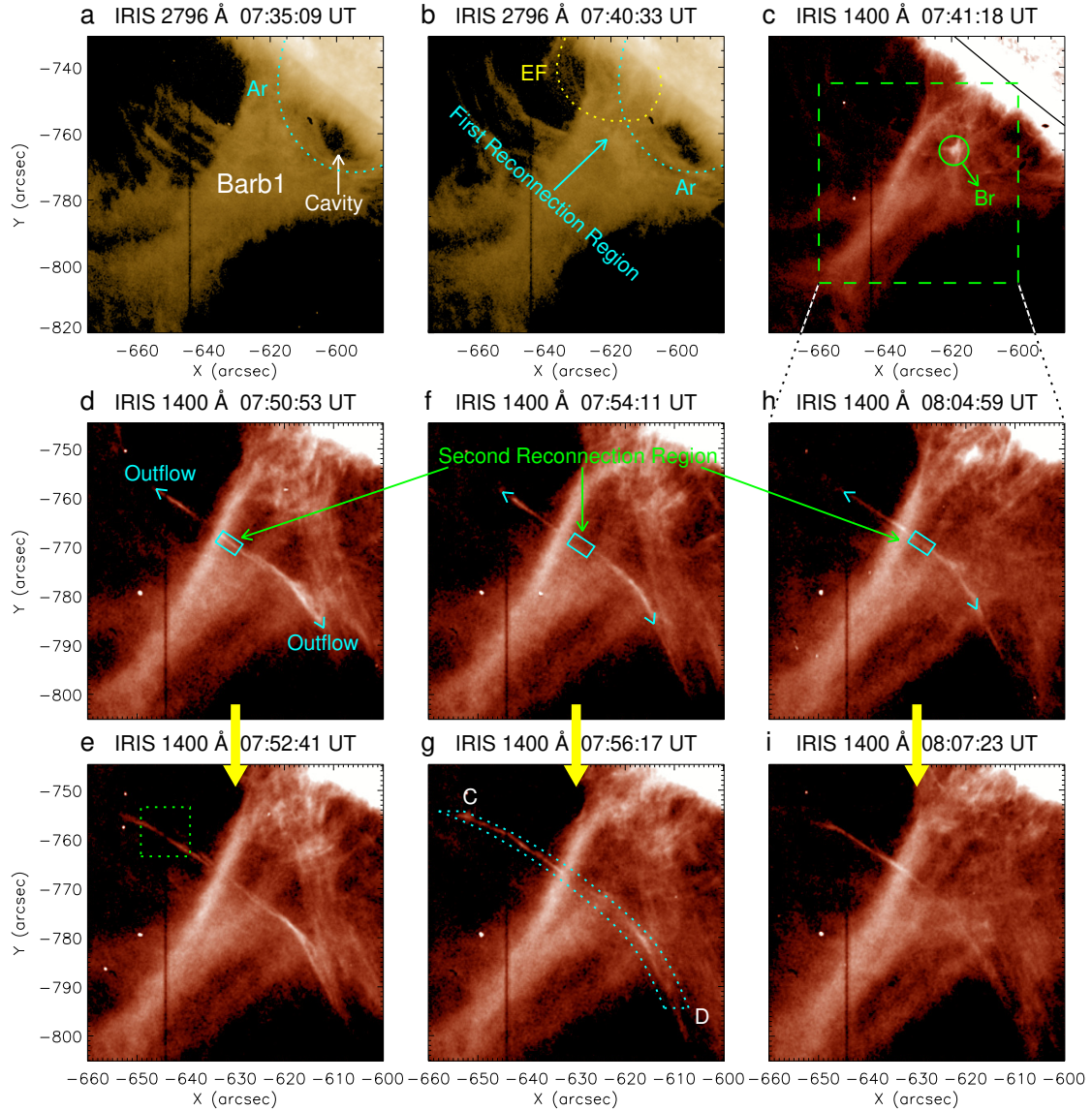


Figure 3. IRIS SJI observation of EF eruption. **a–c**, The early evolution of the eruption in the IRIS 2796 Å (at $T = 0.01$ MK) and 1400 Å (at $T = 0.08$ MK) channel. The square in **c** corresponds to the FOV of panels **d–i**. **d–i**, Three pairs of bidirectional outflows due to the intermittent reconnections between the fields of EF and magnetic dip in Barb1. The square in **e** is the FOV of panels **d** and **g** in Fig. 5. The curved cut in **g** indicates the slit “C–D” along which the 1400 Å time-distance map was plotted in panel **d** of Fig. 4. See Supplementary Video 3.

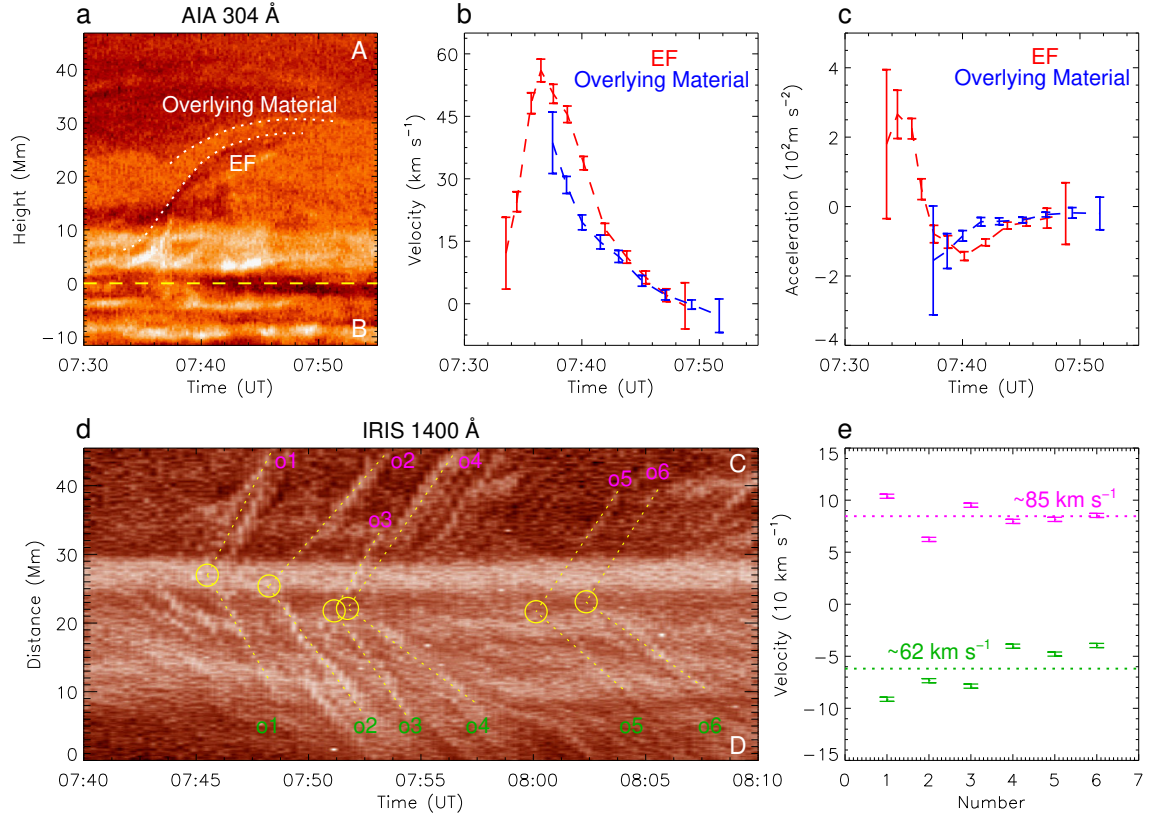


Figure 4. Dynamics of the erupting filament EF in AIA 304 Å at $T = 0.05$ MK and the IRIS SJI bidirectional outflows. **a**, The AIA 304 Å time-distance map shows the height variations of EF and the overlying compressed prominence material in Barb1 during the eruption. The yellow dashed horizontal line indicates the solar surface. **b**, The velocity-time profiles of EF (red) and the overlying prominence material (blue). **c**, The time variations of the accelerations of EF (red) and the compressed prominence material (blue). **d**, IRIS 1400 Å time-distance slit image (at $T = 0.08$ MK) enhanced by the MGN method presents six pairs of bidirectional outflows. The circles mark the spots where the outflows originated. **e**, The projected velocity distribution of the outflows. The purple and green dotted lines represent the mean velocities of the outflows moving toward C and D, respectively.

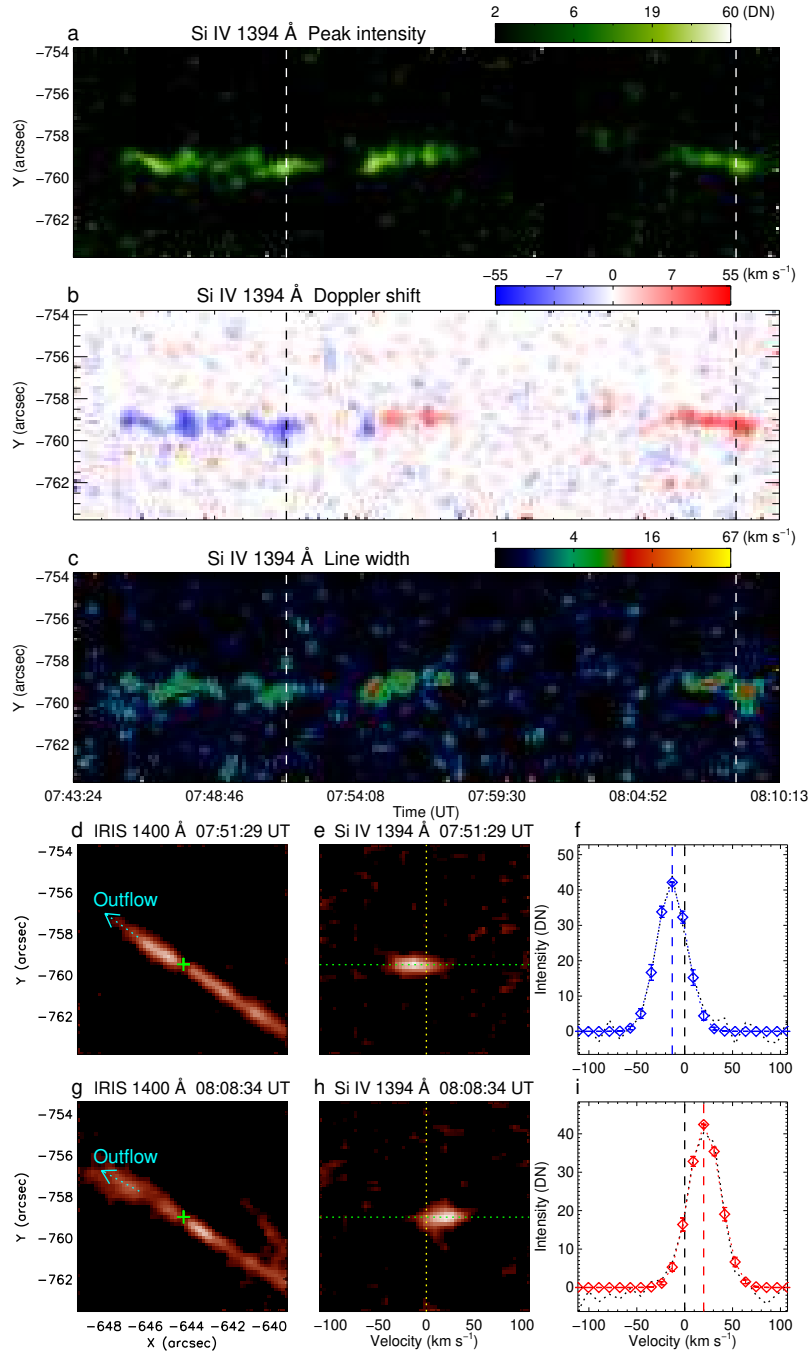


Figure 5. IRIS spectral observations of the outflow. **a–c**, Temporal evolutions of peak intensity, Doppler shift and line width derived from a single-Gaussian fitting to the spectra of Si IV 1393.78 Å line at $T = 0.08$ MK. The two vertical lines in **a**, **b** and **c** indicate the time when the two outflows in **d** and **g** were observed by IRIS. **d–f**, The IRIS 1400 Å imaging data, Si IV 1394 Å line spectrum and profile of the outflow at 07:51:29 UT, respectively. **g–i**, The IRIS 1400 Å imaging data, Si IV 1394 Å line spectrum and profile of the outflow at 08:08:35 UT, respectively. The plus signs in **d** and **g** mark the sites where the outflows crossed the spectrometer slit.

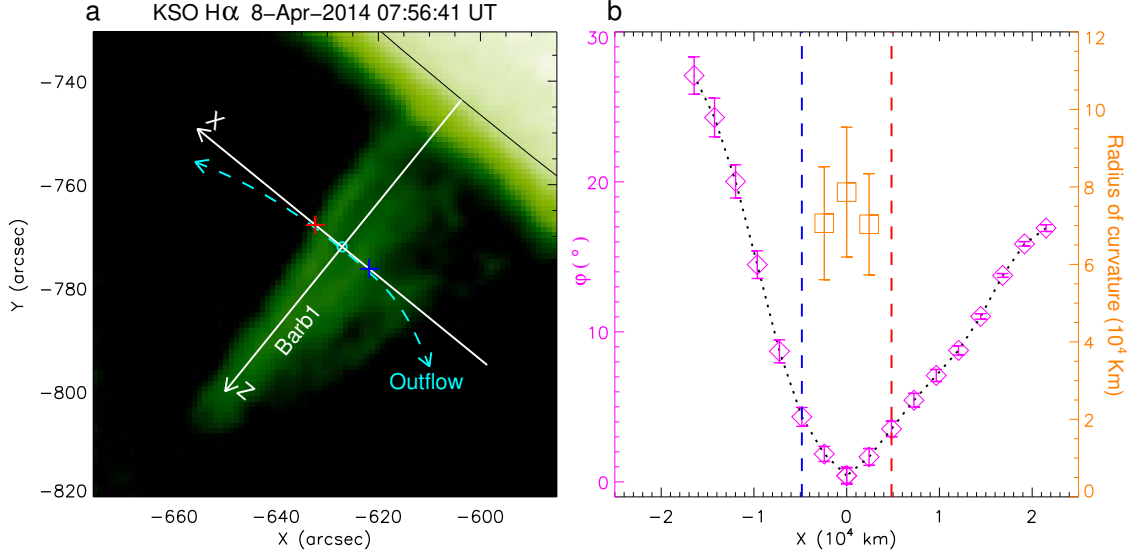


Figure 6. The field orientation of the magnetic dip indicated by outflows across Barb1. **a**, The profile of the bidirectional outflows at 07:56:17 UT overlaid on the KSO H α intensity data at $T < 0.01$ MK. X- and z- axes represent the local horizontal and vertical directions, respectively. **b**, The variations of the angle (ϕ , diamond) between the dip field and x-axis and the curvature radius (square) projected in the plane of the sky of the dip bottom. The plus signs in **a** and vertical lines in **b** indicate the borders of Barb1.

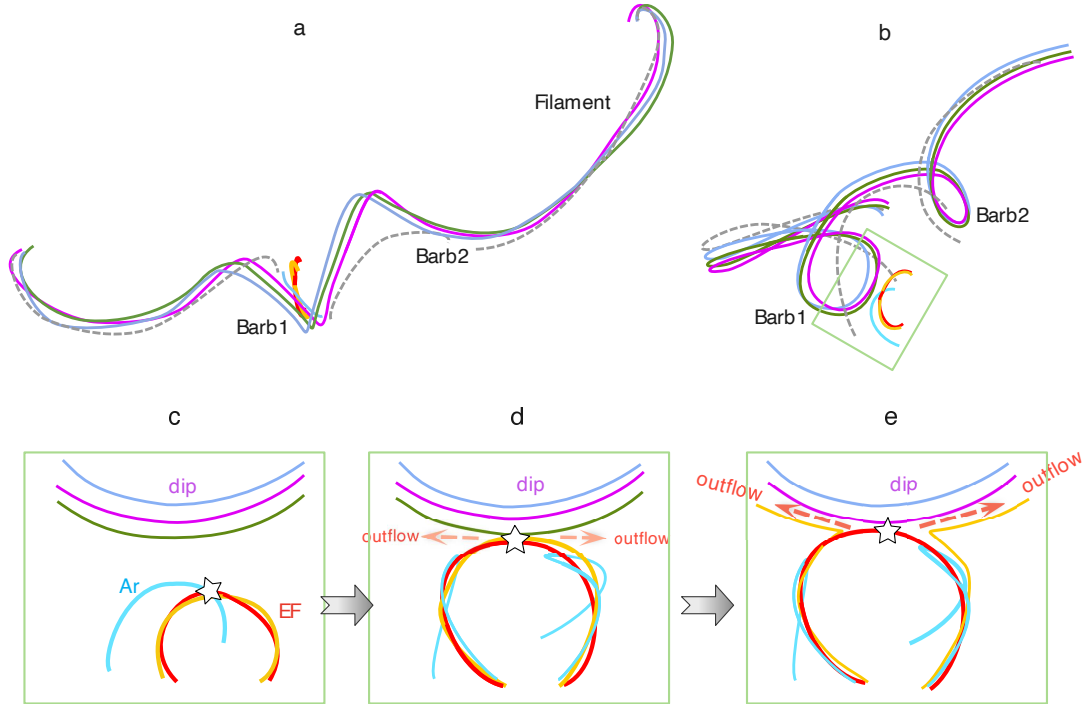


Figure 7. Schematic diagram of magnetic field structure of the larger-scale filament and its reconnection with the fields of EF under Barb1. **a–b**, Top- and side-view of the filament field structure, respectively. **c–e**, The eruption of EF and its interactions with Ar and magnetic dip in Barb1. The box in **b** marks the FOV of panels **c–e**.

Supplementary Files

This is a list of supplementary files associated with this preprint. Click to download.

- [Supplementaryinformation.docx](#)
- [video1.mov](#)
- [video2.mp4](#)
- [video3.mp4](#)